A Triple Phase-Shift Based Control Method for RMS Current Minimization and Power Sharing Control of Input-Series Output-Parallel Dual Active Bridge Converter

Garry Jean-Pierre[1], Mehdy Khayamy[1], Necmi Altin[2], Ahmad El Shafei[1], and Adel Nasiri[1]

[1] Center for Sustainable Electrical Energy Systems, University of Wisconsin-Milwaukee (UWM)
[2] Department of Electrical & Electronics Engineering, Faculty of Technology, Gazi University, Ankara, Turkey
jeanpie4@uwm.edu, mkhayamy@uwm.edu, naltin@gazi.edu.tr, aie@uwm.edu, nasiri@uwm.edu

***Abstract*—High frequency modular power converters are increasingly becoming popular due to their small size and weight. Targeting the input-series and output-parallel (ISOP) dual active bridge (DAB) DC-DC converters, this paper proposes a control scheme based on optimal triple phase-shift (TPS) control for both power sharing control and RMS current minimization. This achieves balanced power transmission, even under mismatched leakage inductance of a DAB module of the ISOP. In order to obtain the optimal zones of operation for the converter, the RMS current was minimized using the Lagrange multiplier method to obtain the optimal duty cycles. The power balancing was added to compensate unbalanced power sharing for variations in model parameters or module shutdown. Analyses and simulation results through MATLAB/Simulink are presented to validate the proposed controller.**

Keywords—Dual active bridge, loss, multi-level, power sharing.

I. Introduction

Modular converters are becoming increasingly attractive due to increased demand for compact and highly efficient isolated DC-DC power converters for different applications, such as fast chargers, uninterruptible power supplies (UPSs), photovoltaic systems and solid state transformers. These structures can be formed by cascading multiple modules of DABs in different configurations, such as input-parallel output-series (IPOS) [1]- [2] and ISOP [3]- [8] or both IPOS and ISOP combined into a single converter [9]. When considering the ISOP configuration, different control strategies have been proposed for balancing the input and regulating the output voltages. The control method for a single module of the converter can either use single phase-shift (SPS), dual phase-shift (DPS), extended phase-shift (EPS) or triple phase-shift (TPS). In [3], a decoupling control method was applied in order to both obtain voltage sharing between the modules and to control the output voltage. A decoupled input and output voltage controller was proposed in [4]. In [5], another decoupled control method was applied to balance the input and regulate the output voltages based on lag compensators. A surge voltage suppression technique was presented in [6] to achieve high power and efficiency for wide load range. However, this method used SPS for power flow between the inputs and the output. Therefore, this method is unable to achieve the maximum efficiency of the system. An input voltage sharing strategy was presented in [7]- [8] to enable proper operation of the converter. All the above mentioned articles, except [6], used the small signal analysis of each module of the ISOP to implement their control method. Advanced control techniques, such as DPS, EPS and TPS, were proposed in [10]-[17] to improve efficiency and to decrease the RMS current, the reactive power loss and the peak current stress.

To further improve upon the control techniques presented in [10]-[17], this paper presents a control scheme based on optimal TPS control for both power sharing control and RMS current minimization. The goal is to achieve balanced power transmission, even under mismatched leakage inductance or shutdown of a DAB module of the ISOP. This work has analyzed all the operation modes and zones of the converter in order to obtain the best operation region for achieving high efficiency.

II. ISOP DAB Converter Analysis and Regions of Operation

A. ISOP DAB Analysis

A standard ISOP DAB converter is shown in Fig. 1. The ISOP is composed of multiple cells configured through series inputs and parallel outputs. Fig. 2 shows the AC side voltage of the first and second bridge voltages, V_1 and V_2, respectively, and the inductor current, I_L, for one cell of the ISOP. D_1 and D_2 are the duty cycles of the first and second converters, respectively, and φ is the phase-shift between V_1 and V_2. All three parameters are defined in per-unit. $D_1 = D_2 = 1$ is the case of the square wave and φ = 1 is 90∘ phase-shift. The simplest method of operation of DAB is considering $D_1 = D_2 = 1$ and adjusting φ to regulate the power. This method covers the entire power capability range of the DAB, and the RMS current is at the minimum for the same voltage level $V_1 = V_2$. However, when V_1 differs from V_2, unnecessary RMS current and the circulating power generate losses and heat the converters and the transformer. The most general and flexible method of operating DAB is to vary all three parameters, D_1, D_2, and φ. Depending on the values of these three variables, V_1 and V_2 waveforms are different, and hence, the calculation is different. To start the calculation of the current and power, all of the possible modes or operation regions should be determined.

B. Regions of Operation

In Fig. 2, the rising and falling times of V_1 and V_2 are defined as x_1 and x_2. y_1 and y_2 are the rising and falling times of V_2 and y_3 is the rising up from negative of V_2.

$$x_1 = 1 - D_1 \tag{1a}$$
$$x_2 = 1 + D_1 \tag{1b}$$
$$y_1 = 1 - D_2 + \varphi \tag{1c}$$
$$y_2 = 1 + D_2 + \varphi \tag{1d}$$
$$y_3 = -1 + D_2 + \varphi \tag{1e}$$

When considering the half of the period which contains x_1 and x_2, there are three areas in which y_1, y_2, and y_3 can lay. However, it is impossible to have $y_3 > x_2$, as it is a logical contradiction. Knowing $y_3 < x_2$ eliminates a set of possibilities which are not feasible.

$$y_3 > x_2 \tag{2a}$$
$$-1 + D_2 + \varphi > 1 + D_1 \tag{2b}$$
$$-D_1 + D_2 + \varphi > 2 \rightarrow \perp \tag{2c}$$

y_3 and y_1 cannot exist at the same time in half a period. The fact that only y_1 and y_2 or y_3 and y_1 can happen at the same time removes several possible combinations.

$$y_3 > 0 \ \ \& \ \ y_2 < 2 \tag{3a}$$
$$-1 + D_2 + \varphi > 0 \ \ \& \ \ 1 + D_2 + \varphi < 2 \tag{3b}$$
$$D_2 + \varphi > 1 \ \ \& \ D_2 + \varphi < 1 \rightarrow \perp \tag{3c}$$

Unlike the previous impossible combinations which describe a set of possibilities, this combination is a specific case which is a logical contradiction.

$$y_1 < x_1 \ \ \& \ \ y_2 < x_2 \tag{4a}$$
$$1 - D_2 + \varphi < 1 - D_1 \ \ \& \ 1 + D_2 + \varphi < 1 + D_1 \tag{4b}$$
$$\text{Add}: 2 + 2\varphi < 2 \rightarrow \varphi < 0 \rightarrow \perp \tag{4c}$$

This condition describes another specific impossible case:

$$y_3 > x_1 \ \ \& \ \ y_1 > x_2 \tag{5a}$$
$$-1 + D_2 + \varphi > 1 - D_1 \ \& \ 1 - D_2 + \varphi > 1 + D_1 \tag{5b}$$
$$\text{Add}: 2\varphi > 2 \rightarrow \varphi > 1 \rightarrow \perp \tag{5c}$$

All of the remaining feasible possible combinations are considered for the derivation of the equations. The names of each region come from the three dimensional regions in which each condition is satisfied. Fig. 3 shows one example waveform of each region. Figs. 3(a) - 3(e) show the primary and secondary voltage of the transformer, V_1 and V_2, respectively. Figs. 3(f)- 3(j) are the resultant currents passing through the transformer from one converter to another and Figs. 3(k)- 3(o) illustrate the instantaneous power sent from the first converter. Figs. 3(p)- 3(t) are feasible regions in a 3D space of D_1, D_2, and φ. Derivation of the "Right" (Orange) region is presented here. The other regions are derived similarly. The conditions for this region are as follows:

$$x_1 < y_1 \ \& \ y_2 < x_2 \tag{6a}$$
$$1 - D_1 < 1 - D_2 + \varphi \ \& \ 1 + D_2 + \varphi < 1 + D_1 \tag{6b}$$
$$-D_1 + D_2 - \varphi < 0 \ \& \ -D_1 + D_2 + \varphi < 0 \tag{6c}$$
$$-D_1 + D_2 + \varphi < 0 \tag{6d}$$

The boundaries of all the regions are listed in Table I.

III. RMS Current and Average Power Derivation

The first step in calculating the RMS current and average power is to formulate the instantaneous expressions. The magnetizing current of the transformer is neglected in comparison to the leakage current. The instantaneous current is calculated piecewise for each region of operation based on (7).

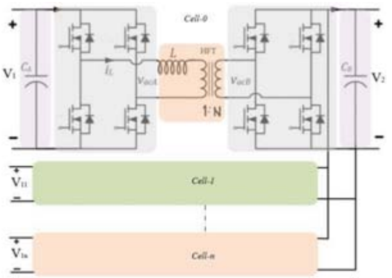

Fig. 1. ISOP DAB converter

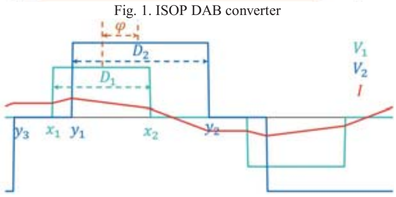

Fig. 2. DAB AC voltage and inductor current

Table I. Boundary Regions

Front	$D_1 + D_2 - \varphi < 0$
Right	$-D_1 + D_2 + \varphi < 0$
Left	$D_1 - D_2 + \varphi < 0$
Middle	$0 \leq D_1, D_2, \varphi \leq 1$
Rear	$D_1 + D_2 + \varphi > 2$

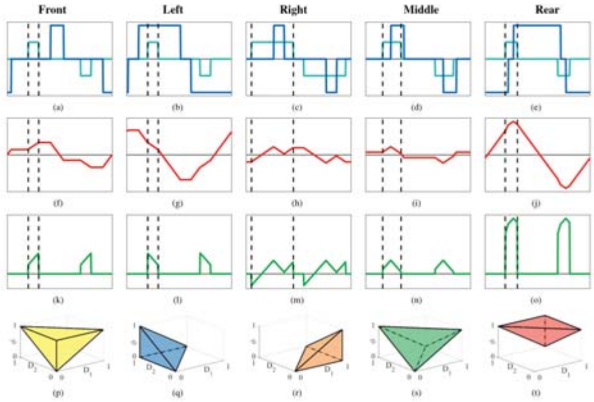

Fig. 3. Waveform of various modes of operation: (a) - (e) AC side voltages of the first and second converters; (f) - (j) the current from the first converter to the second; (k) - (o) power flow from the first converter to the second; and (p) - (t) boundaries of regions of the operation.

$$I_l(t) = I_0 + \frac{1}{L}\int_{Z_A}^{Z_B}(V_1(t) - V_2(t))dt \tag{7}$$

In (7), z_A and z_B can be 0, x_1, x_2, y_1, y_2, y_3, or 2, depending on the region of operation and the piece of the current. The output current may not be vertically symmetrical. However, after the transient, the current is symmetric around the x axis. Hence, the average of the current needs to be calculated and subtracted from the instantaneous current. The average calculation has been done in a piecewise manner in (8).

$$I_{ave} = \Sigma_{(i=1)}^{8}\int_{Z_{A_i}}^{Z_{B_i}} I(t)dt \tag{8}$$

The average power is calculated piecewise in each region from (9), where V_1 and I are variables, depending on the piece in each region. The RMS current is obtained from (10).

$$P_{ave} = \Sigma_{(i=1)}^{8} V_1(t)\int_{ZAi}^{ZBi}(I(t) - I_{ave})dt \tag{9}$$
$$I_{rms} = \sqrt{\left(\Sigma_{(i=1)}^{8}\int_{Z_{A_i}}^{Z_{B_i}}(I(t) - I_{ave})dt\right)^2} \tag{10}$$

The average power equation for each region is obtained in (11). $P_{aveFront}$, $P_{aveRight}$ and, $P_{aveLeft}$ are independent to φ, D_1, and D_2, respectively, as they could be predicted by examining Figs. 3(a)- 3(c).

$$P_{aveFront} = \frac{V_1V_2}{8LF}2D_1D_2 \tag{11a}$$
$$P_{aveRight} = \frac{V_1V_2}{8LF}2D_2\varphi \tag{11b}$$
$$P_{aveLeft} = \frac{V_1V_2}{8LF}2D_1\varphi \tag{11c}$$
$$P_{aveMiddle} = \frac{V_1V_2}{8LF}\begin{pmatrix} -\frac{1}{2}(D_1 - D_2)^2 \\ +\varphi(D_1 + D_2 - ½\,\varphi)\end{pmatrix} \tag{11d}$$
$$P_{aveRear} = \frac{V_1V_2}{8LF}\begin{pmatrix} -(D_1^2 + D_2^2) - 2 \\ +2(D_1 + D_2) + \varphi(2 - \varphi)\end{pmatrix} \tag{11e}$$

The expression of the average powers after the common term of $\frac{V_1V_2}{8Lf}$ is the per-unit power. The following conclusions can be made from the maximum achievable per-unit power as in (12):

$$\text{Max}_{\text{PpuFront}} = 0.5 \quad \text{at} \quad (D_1 = D_2 = 0.5) \tag{12a}$$
$$\text{Max}_{\text{PpuRight}} = 0.5 \text{ at } (D_2 = \varphi = 0.5) \tag{12b}$$
$$\text{Max}_{\text{PpuLeft}} = 0.5 \text{ at } (D_1 = \varphi = 0.5) \tag{12c}$$

$\text{Max}_{\text{PpuMiddle}} = 0.5$ at $(D_1 = D_2 = 0.5, \varphi = 1)$ (12d)

$\text{Max}_{\text{PpuRear}} = 1.0$ at $(D_1 = D_2 = \varphi = 1)$ (12e)

There is a common term between all of the RMS current equations which is written in (13). The RMS currents for all of the regions are obtained in (14). Although some average powers are independent to some variables, all of the variables affect RMS current in all of the regions.

$$I_{com} = \frac{V_1}{V_2}\left(\frac{3}{2}D_1^2 - D_1^3\right) + \frac{V_2}{V_1}\left(\frac{3}{2}D_2^2 - D_2^3\right) \tag{13}$$

$$I_{rmsFront} = \frac{\sqrt{V_1V_2}}{2\sqrt{2}\,LF}\left(I_{com} + 3D_1D_2(\varphi - 1)\right)^{\frac{1}{2}} \tag{14a}$$

$$I_{rmsRight} = \frac{\sqrt{V_1V_2}}{2\sqrt{2}\,LF}\begin{pmatrix} I_{com} + \frac{1}{2}D_2^3 + \frac{3}{2}D_1^2 D_2 \\ + \frac{3}{2}D_2\varphi^2 - 3D_1 D_2 \end{pmatrix}^{\frac{1}{2}} \tag{14b}$$

$$I_{rmsLeft} = \frac{\sqrt{V_1V_2}}{2\sqrt{2}\,LF}\begin{pmatrix} I_{com} + \frac{1}{2}D_1^3 + \frac{3}{2}D_1D_2^2 \\ + \frac{3}{2}D_1\varphi^2 - 3D_1 D_2 \end{pmatrix}^{\frac{1}{2}} \tag{14c}$$

$$I_{rmsMiddle} = \frac{\sqrt{V_1V_2}}{2\sqrt{2}\,LF}\begin{pmatrix} I_{com} + \frac{1}{4}(D_1^3 + D_2^3) + \frac{3}{4}D_1 D_2(D_1 + D_2) \\ -3D_1D_2 + \frac{3}{2}D_1D_2\varphi - \frac{3}{4}(D_1^2 + D_2^2)\varphi \\ + \frac{3}{4}(D_1 + D_2)\varphi^2 - \frac{1}{4}\varphi^3 \end{pmatrix}^{\frac{1}{2}} \tag{14d}$$

$$I_{rmsRear} = \frac{\sqrt{V_1V_2}}{2\sqrt{2}\,LF}\begin{pmatrix} I_{com} + \frac{3}{2}(D_1^2 + D_2^2) \\ -3(D_1 + D_2) + 3(D_1 + D_2)\varphi \\ -\frac{3}{2}(D_1^2 + D_2^2)\varphi - 3\varphi\,\frac{3}{2}\varphi^2 - \frac{1}{2}\varphi^3 + 2 \end{pmatrix}^{\frac{1}{2}} \tag{14e}$$

IV. Optimized Trajectories

The goal of the optimization is to minimize RMS current for a given average power. The variables are D_1, D_2, and φ. The objective function, f, is the RMS current which needs to be minimized. The constraint, g, is the average power which the converter should be able to provide, regardless of the current. The Lagrange Multiplier method is used for the constraint optimization problem of the DAB. Based on Lagrange optimization methodology, a Lagrange function is the combination of the objective function and the constraint multiplied by λ, as formulated in (15).

$$\Lambda(D_1, D_2, \varphi, \lambda) = f(D_1, D_2, \varphi) + \lambda_g(D_1, D_2, \varphi) \tag{15}$$

The optimal solution of the constraint optimization is described by a set of equations of the gradient of the Lagrange Multiplier, as written in (16) for the DAB. Although $\partial\Lambda/\partial\lambda = 0$ is part of $\nabla\Lambda = 0$, it does not reveal any new information, as it is simply the constraint function, g, itself.

$$\nabla\Lambda = 0 \rightarrow \frac{\partial\Lambda}{\partial D_1} = 0 \;\&\; \frac{\partial\Lambda}{\partial D_2} = 0 \;\&\; \frac{\partial\Lambda}{\partial\varphi} = 0 \tag{16}$$

There are five regions and each has its own f, g, and Λ. As shown in (16), there are three equations with four unknowns, which means there is a relation between the variables rather than an exact value. To find the optimal trajectory in each region, λ needs to be found from one of the three equations of (16) and substituted in the others. The expression φ should be calculated from one of the remaining equations and substituted in the others. The last equation reveals the relation between D_1 and D_2 and this relation should be substituted back into the φ expression. If the relation describes a trajectory outside of the boundary of a region, the boundary is the best feasible solution.

The derivations of the optimal trajectories for all of the regions have been done, but for each set of conditions the optimal RMS current of one of the regions is minimum. Only the derivation of the best region is presented here. Since the only region that can cover powers above 0.5*pu* is the Rear region, the comparison of regions has been done only up to 0.5*pu*. For power higher than 0.5*pu*, only the optimal trajectory in the Rear region needs to be derived. Fig. 4(b) shows the minimum RMS current that each region can provide for the range of per-unit power of 0- 0.5. In this figure, $V_1 = V_2$ and the best result is the Rear (red) region. The corresponding trajectory in the Rear region is shown in Fig. 4(r), where $D_1 = D_2 = 1$, which is the square wave operation. The optimal trajectories in the other regions for this condition are shown in Figs. 4(f), 4(l), 4(m), and 4(g). Fig. 4(s) shows the optimal trajectory regardless of region, which is identical to the optimal trajectory of the Rear region in this case. This means if the DAB is being used only for isolation purpose with $V_1 = V_2$, then the square wave operation is the optimal operation.

Fig. 4(c) shows the minimum RMS current when $V_2 > V_1$. The Right and Middle regions have the minimum current and exactly the same value. In Figs. 4(n) and 4(i), the optimal trajectory lies on the boundary of the Right and Middle regions, which explains why they have the same current. The Left region has the highest current. After 0.5*pu,* the only optimal trajectory is the Rear region of Fig. 4(t). Fig. 4(u) shows the overall trend that the optimal trajectory should be on the boundary of the Left and Right regions: $-D_1 + D_2 + \varphi = 0$ plane. For higher power, when D_1 is saturated to 1, it is on the $D_1 = 1$ plane. Eventually, when both D_1 and D_2 are saturated, it is on $D_1 = D_2 = 1$ line. A dual situation is shown in Fig. 4(a) when $V_2 < V_1$. The optimal trajectory for $P < 0.5\,\pi$ is the boundary of the Left and Middle regions or $D_1 - D_2 + \varphi = 0$ plane. For higher power, D_2 would be saturated to 1 and the trajectory is on $D_2 = 1$ plane up to the point where D_1 becomes saturated as well. The last part of the optimal trajectory is on $D_1 = D_2 = 1$ line. It can be observed that the optimal trajectory of any condition is never inside of a region, but always on the surface or boundary of the regions.

V. Control Structure

There are three zones on the optimal trajectory, as shown in Fig. 5. (a) These zones are discussed below. The relation of each zone and the boundary between them is derived and shown in Fig. 5. (b)- (d).

A. Zone 1

The first zone is low power when D_1 & $D_2 \leqslant 1$. For $V_2 > V_1$, the optimal trajectory is on $-D_1 + D_2 + \varphi = 0$. Based on the Lagrange Optimization, $V_1D_1 = V_2D_2$.

$$\varphi = D_1 - D_2 \tag{17a}$$

$$\varphi = D_1 - \frac{V_1}{V_2}D_1 \tag{17b}$$

$$D_{1z_1V_2>V_1} = \frac{V_2}{V_2 - V_1}\varphi \tag{17c}$$

$$D_{2z_1V_2>V_1} = \frac{V_1}{V_2 - V_1}\varphi \tag{17d}$$

The trajectory lies on the boundary of the Right and Middle regions, so the power equation of either of them can be used. The per-unit power is shown in (18).

$$P_{z_1V_2>V_1} = 2D_2\varphi \tag{18a}$$

$$P_{z_1V_2>V_1} = \frac{2V_1}{V_2 - V_1}\varphi^2 \tag{18b}$$

This zone ends when $D_1 = 1$, which means $\varphi = \frac{V_2 - V_1}{V_2}$. Substituting this φ into (18) yields P_{12}, the power at the boundary of zones 1 and 2.

$$P_{12V_2>V_1} = 2V_1\frac{V_2 - V_1}{V_2^2} \tag{19}$$

The case of $V_2 < V_1$ is a dual of $V_2 > V_1$.

$$D_{2z_1V_2<V_1} = \frac{V_1}{V_1 - V_2}\varphi \tag{20a}$$

$$D_{1z_1 V_2<V_1} = \frac{V_2}{V_1-V_2}\varphi \tag{20b}$$
$$P_{z1V2} < V = \frac{2V_2}{V_1-V_2}\varphi^2 \tag{21}$$
$$P_{12V_2<V_1} = 2V_2\frac{V_1-V_2}{V_1^2} \tag{22}$$

B. Zone 2

The second zone is medium power when D_1 is reached to the limit of 1 for $V_2 > V_1$. The optimal trajectory is $D_1 = 1$ plane. By solving the Lagrange Multiplier in the Rear region and eliminating two of the equations via substitution, (23) can be derived. This is the solution of a quadratic equation which relates D_2 to φ.

$$D_2^2 + \left(-2 - \frac{2V_2}{V_1(\varphi-1)}\right)D_2 + (-\varphi^2 + 2\varphi - 1) = 0 \tag{23a}$$
$$D_{2z_2V_2>V_1} = \frac{V_2}{V_1}(\varphi-1) + 1 + \sqrt{\left(\frac{V_2}{V_1}(\varphi-1)+1\right)^2 + \varphi^2 - 2\varphi + 1} \tag{23b}$$

Substituting $D_1 = 1$ and D_2 from (23) into the Rear region power equation gives the power in zone 2. This zone ends when $D_2 = 1$:

$$P_{23\,V_2>V_1} = 2 - 2\left(\frac{V_2}{V_1}\right)^2 + \frac{2V_2}{V_1}\sqrt{\left(\frac{V_2}{V_1}\right)^2 - 1} \tag{24}$$

Similarly, for the dual case of $V_2 < V_1$ the following equations can be derived.

$$D_1^2 + \left(-2 - \frac{2V_1}{V_2}(\varphi-1)\right)D_1 + (-\varphi^2 + 2\varphi - 1) = 0 \tag{25a}$$
$$D_{1z_2V_2<V_1} = \frac{V_1}{V_2}(\varphi-1) + 1 + \sqrt{\left(\frac{V_1}{V_2}(\varphi-1)+1\right)^2 + \varphi^2 - 2\varphi + 1} \tag{25b}$$
$$\varphi = -\frac{V_1}{V_2} + 1 + \sqrt{\left(\frac{V_1}{V_2}\right)^2 - 1} \tag{26a}$$
$$P_{23\,V_2<V_1} = 2 - 2\left(\frac{V_1}{V_2}\right)^2 + \frac{2V_1}{V_2}\sqrt{\left(\frac{V_1}{V_2}\right)^2 - 1} \tag{26b}$$

C. Zone 3

The third and last zone is the high power zone when both D_1 and D_2 are saturated to 1. Varying φ is the only way to increase the power. Regardless of the relation between V_1 and V_2, the per-unit power in this zone has the same equation of the square wave. This can be found by substituting $D_1 = D_2 = 1$ into the power equation of the Rear region, as is written in (27).

$$P_{z_3} = \varphi(2-\varphi) \tag{27}$$

The optimal closed loop control block diagram is shown in Fig. 6. PI controllers generate the duty cycles and phase-shift variation that compensate the power variation, which can occur in cases of mismatched transformer leakage inductance or when one converter is shut down. These variations are incremented to the optimal duty cycles in order to produce the final optimal D_1, D_2 and φ.

VI. Simulation Results

Fig. 7- 9 show the simulation results for the ISOP. Four scenarios are considered based on Fig. 5(a). Table II presents a summary of the simulation results. Fig. 7 (a)- (c) show the independent and total powers, the primary and secondary voltages and the leakage inductor currents of the transformer, and the output voltage with the three independent RMS currents of the three DAB cells of the ISOP. This was done with the system balanced under SPS control method, which is the ideal AC square wave voltage case. Fig. 7 (d)- (f) present the same powers, voltages and current waveforms when the TPS optimization control method is applied. It can be seen that the proposed control method effectively decreases the RMS current of the system. Fig. 7 (g)- (i) show the key voltage and leakage current for each operating zone of Fig. 4. From 0.4 to 0.6 seconds, the converter of Cell-1 is shut down. To compensate for this power deficit, the other two operating converters increase their power level to meet the load requirement. To further validate the power sharing algorithm, 25% mismatch leakage inductance is introduced in the converter of Cell-1. In this scenario, the algorithm changes the phase-shift and the duty cycles of the unbalance cell in order to keep the ISOP balanced. This can be seen in Fig. 8 (a) and (c). However, Fig. 9 shows the performance of the ISOP without the power sharing method. It can be seen that Cell-1 power is less than the other two DAB cells, meaning the system is unable to meet the load requirement.

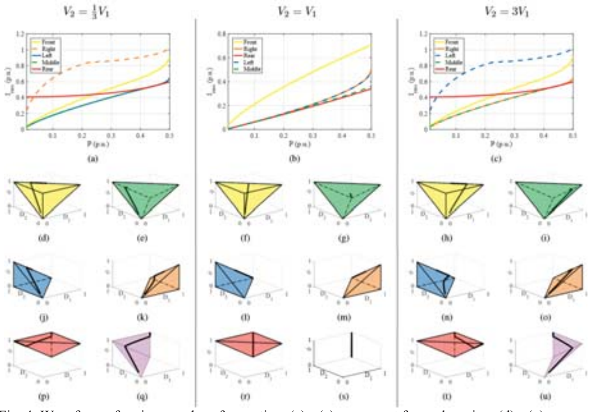

Fig. 4. Waveform of various modes of operation: (a) - (c) pu current for each region; (d) - (u) optimal trajectory of D_1, D_2 and φ

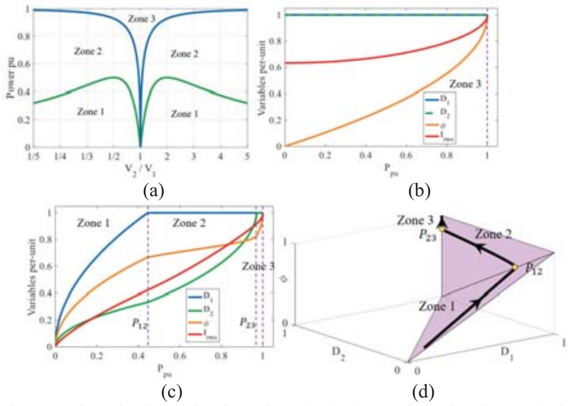

Fig. 5. Waveform of various modes of operation: (a) optimal zones of operation. (b)-(c) optimal pu value for D_1, D_2 and φ. (d) optimal trajectory of D_1, D_2 and φ

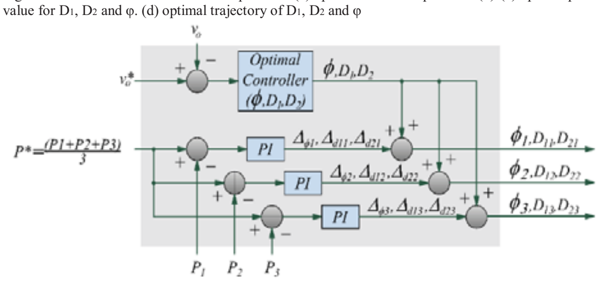

Fig. 6. Optimal closed loop control block diagram for the three cells DAB system

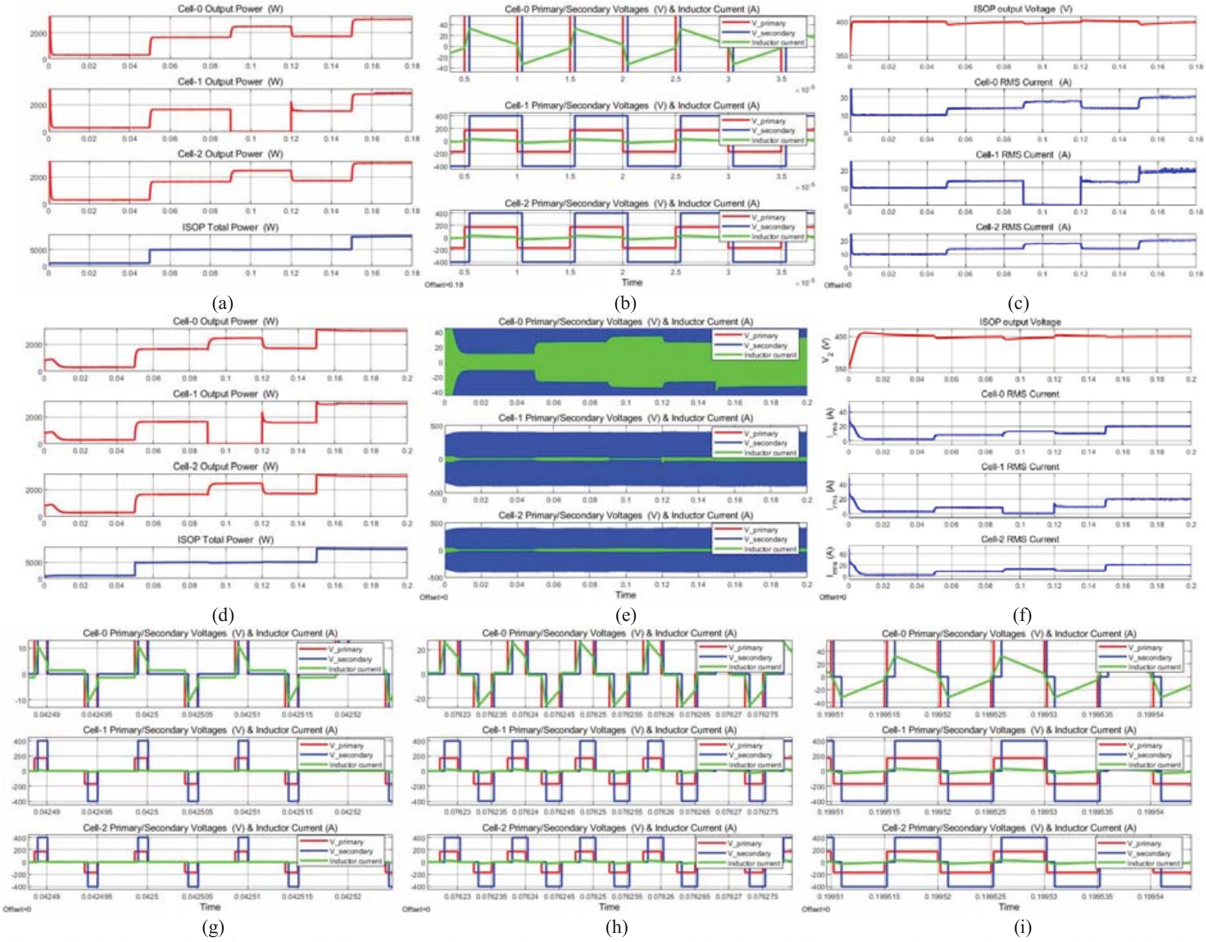

Fig. 7. Simulation results of the ISOP: (a)-(c) powers, voltages and currents with no optimization, (d)-(f) powers, voltages and currents with optimization, (c) voltages and inductor currents for each power zone (g) zone 1, (h) zone 2, (i) zone 3.

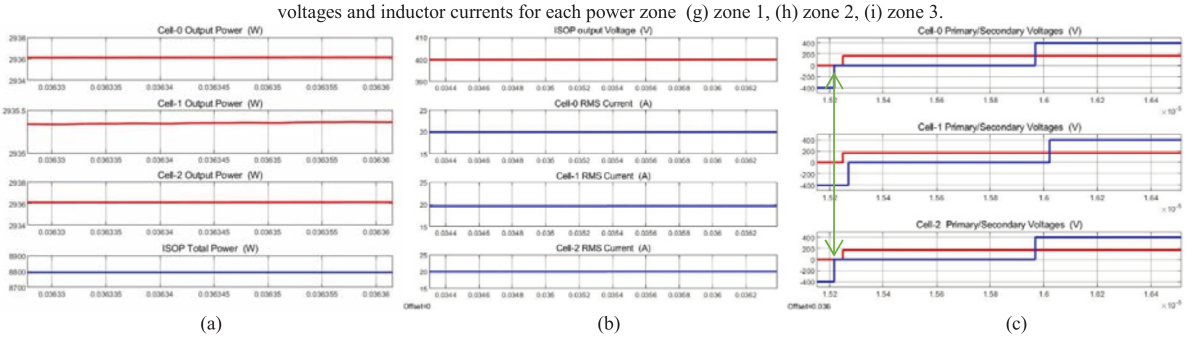

Fig. 8. Performance results of the ISOP with power sharing method under mismatched leakage inductance. (a) powers, (b) RMS currents (c) primary and secondary voltages and leakage currents

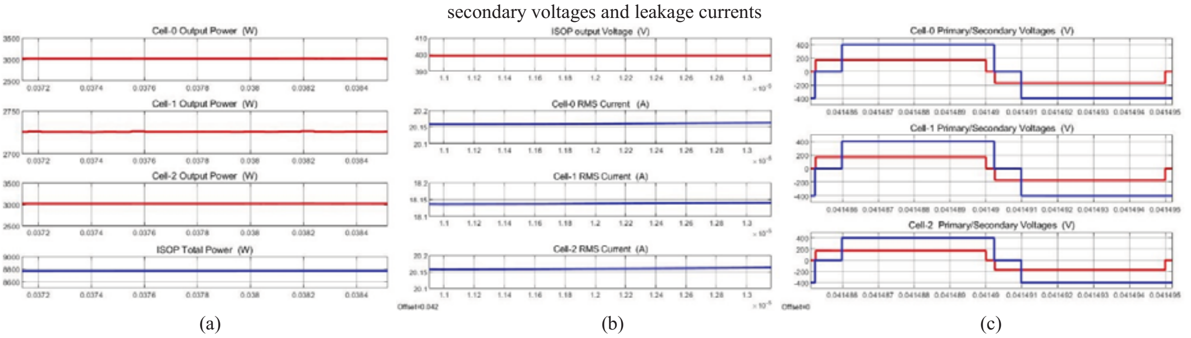

Fig. 9. Performance results of the ISOP without power sharing method under mismatched leakage inductances. (a) powers, (b) RMS currents (c) primary and secondary voltages and leakage currents

TABLE. II SUMMARY OF SIMULATION RESULTS

	ISOP SPS control without optimization				ISOP TPS control with optimization			
Zone	1	2	1-2/2-3	3	1	2	1-2/2-3	3
Time (s)	0 – 0.05	0.05- 0.09	0.09 -0.12	0.15- 0.2	0 – 0.05	0.05- 0.09	0.09 -0.12	0.15- 0.2
Power Level	Low	Medium	Power sharing	High	Low	Medium	Power sharing	High
RMS current (A)	10.1	13.9	18.1	22	2.1	8.25	11.8	19.1

VII. CONCLUSION

This paper proposes a power sharing control method added to the RMS current minimization technique based on Lagrange optimization for an ISOP of three modules. The TPS control method has been applied to regulate the ISOP. Detailed analyses of the RMS current and average power transferred in the DAB for each mode and the power sharing controller for all operation zones are presented in the paper. Four scenarios of the simulation results are summarized in Table II. It can be seen that the TPS method has significantly minimized the RMS current of the DAB, especially at low load condition, and improved the efficiency for the overall power range. The power sharing method has been applied to maintain equal power between the converters under various conditions, such as converter shutdown and mismatch in leakage inductance of the transformers. Simulation results have proven the effectiveness of all the control techniques employed.

VIII. ACKNOWLEDGEMENT

This material is based upon work supported by the National Science Foundation under Grant No. 1650470. Any opinions, findings, and conclusions or recommendations expressed in this material are those of the author(s) and do not necessarily reflect the views of the National Science Foundation.

REFERENCES

[1] S. Lee, Y. Jeung and D. Lee, "Voltage Balancing Control of IPOS Modular Dual Active Bridge DC/DC Converters Based on Hierarchical Sliding Mode Control," IEEE Access, vol. 7, pp. 9989-9997, 2019.

[2] C. Jung and D. Lee, "Decoupling Control of Input-Paralleled System with Dual Active Bridge Converters," *2019 International Symposium on Electrical and Electronics Engineering (ISEE)*, Ho Chi Minh, Vietnam, 2019, pp. 226-231.

[3] H. Sun, J. Zhang and C. Fu, "Control strategy for dual active bridge based DC solid state transformer," *2017 20th International Conference on Electrical Machines and Systems (ICEMS)*, Sydney, NSW, 2017, pp. 1-6.

[4] P. Zumel, L. Ortega, A. Lazaro, C. Fernandez and A. Barrado, "Control strategy for modular Dual Active Bridge input series output parallel," *2013 IEEE 14th Workshop on Control and Modeling for Power Electronics (COMPEL)*, Salt Lake City, UT, 2013, pp. 1-7.

[5] F. Deng, X. Zhang, X. Li, T. Lei and T. Wang, "Decoupling Control Strategy for Input-Series Output-Parallel Systems Based on Dual Active Bridge dc-dc Converters," *2018 9th IEEE International Symposium on Power Electronics for Distributed Generation Systems (PEDG)*, Charlotte, NC, 2018, pp. 1-8.

[6] M. Sato *et al.*, "High efficiency design for ISOP converter system with dual active bridge DC-DC converter," *2016 IEEE Applied Power Electronics Conference and Exposition (APEC)*, Long Beach, CA, 2016, pp. 2465-2472.

[7] P. Zumel *et al.*, "Modular Dual-Active Bridge Converter Architecture," *IEEE Transactions on Industry Applications*, vol. 52, no. 3, pp. 2444-2455, May-June 2016.

[8] Y. Wang, K. Wang, C. Li, Z. Zheng and Y. Li, "System-Level Efficiency Evaluation of Isolated DC/DC Converters in Power Electronics Transformers for Medium-Voltage DC Systems," *IEEE Access*, vol. 7, pp. 48445-48458, 2019.

[9] Y. A. Harrye, A. A. Aboushady and K. H. Ahmed, "Power sharing controller for modular dual active bridge DC/DC converter in medium voltage DC applications," *2017 IEEE 6th International Conference on Renewable Energy Research and Applications (ICRERA)*, San Diego, CA, 2017, pp. 602-607.

[10] F. An, W. Song, K. Yang, S. Yang and L. Ma, "A Simple Power Estimation with Triple Phase-Shift Control for the Output Parallel DAB DC–DC Converters in Power Electronic Traction Transformer for Railway Locomotive Application," *IEEE Transactions on Transportation* vol. 5, no. 1, pp. 299-310, March 2019.

[11] H. Bai and C. Mi, "Eliminate Reactive Power and Increase System Efficiency of Isolated Bidirectional Dual-Active-Bridge DC–DC Converters Using Novel Dual-Phase-Shift Control," *IEEE Transactions on Power Electronics*, vol. 23, no. 6, pp. 2905-2914, Nov. 2008.

[12] B. Zhao, Q. Yu and W. Sun, "Extended-Phase-Shift Control of Isolated Bidirectional DC–DC Converter for Power Distribution in Microgrid," *IEEE Transactions on Power Electronics*, vol. 27, no. 11, pp. 4667-4680, Nov. 2012.

[13] A. Tong, L. Hang, G. Li, X. Jiang and S. Gao, "Modeling and Analysis of a Dual-Active-Bridge-Isolated Bidirectional DC/DC Converter to Minimize RMS Current with Whole Operating Range," *IEEE Transactions on Power Electronics*, vol. 33, no. 6, pp. 5302-5316, June 2018.

[14] Y. Shi, R. Li, Y. Xue and H. Li, "Optimized Operation of Current-Fed Dual Active Bridge DC–DC Converter for PV Applications," *IEEE Transactions on Industrial Electronics*, vol. 62, no. 11, pp. 6986-6995, Nov. 2015.

[15] B. Zhao, Q. Song and W. Liu, "Efficiency Characterization and Optimization of Isolated Bidirectional DC–DC Converter Based on Dual-Phase-Shift Control for DC Distribution Application," *IEEE Transactions on Power Electronics*, vol. 28, no. 4, pp. 1711-1727, April 2013.

[16] J. Huang, Y. Wang, Z. Li and W. Lei, "Unified Triple-Phase-Shift Control to Minimize Current Stress and Achieve Full Soft-Switching of Isolated Bidirectional DC–DC Converter," *IEEE Transactions on Industrial Electronics*, vol. 63, no. 7, pp. 4169-4179, July 2016.

[17] N. Hou, W. Song and M. Wu, "Minimum-Current-Stress Scheme of Dual Active Bridge DC–DC Converter with Unified Phase-Shift Control," *IEEE Transactions on Power Electronics*, vol. 31, no. 12, pp. 8552-8561, Dec. 2016.